



ISTITUTO NAZIONALE DI RICERCA METROLOGICA Repository Istituzionale

Finite-Size and Illumination Conditions Effects in All-Dielectric Metasurfaces

Original

Finite-Size and Illumination Conditions Effects in All-Dielectric Metasurfaces / Ciarella, Luca; Tognazzi, Andrea; Mangini, Fabio; De Angelis, Costantino; Pattelli, Lorenzo; Frezza, Fabrizio. - In: ELECTRONICS. - ISSN 2079-9292. - 11:7(2022), p. 1017. [10.3390/electronics11071017]

Availability:

This version is available at: 11696/74379 since: 2022-05-23T07:57:08Z

Publisher:

MDPI

Published

DOI:10.3390/electronics11071017

Terms of use:

This article is made available under terms and conditions as specified in the corresponding bibliographic description in the repository

Publisher copyright

(Article begins on next page)

Article

Finite-Size and Illumination Conditions Effects in All-Dielectric Metasurfaces

Luca Ciarella ^{1,†} , Andrea Tognazzi ^{2,3,*,†} , Fabio Mangini ^{4,†} , Costantino De Angelis ^{3,4,5} ,
Lorenzo Pattelli ^{6,7,†}  and Fabrizio Frezza ^{1,5} 

- ¹ Dipartimento di Ingegneria dell'Informazione, Elettronica e Telecomunicazioni, Sapienza Università di Roma, Via Eudossiana 18, 00184 Roma, Italy; ciarella.1656100@studenti.uniroma1.it (L.C.); fabrizio.frezza@uniroma1.it (F.F.)
 - ² Dipartimento di Ingegneria, Università degli Studi di Palermo, Viale delle Scienze ed. 8, 90128 Palermo, Italy
 - ³ Istituto Nazionale di Ottica-Consiglio Nazionale delle Ricerche (INO-CNR), Via Branze 45, 25123 Brescia, Italy; costantino.deangelis@unibs.it
 - ⁴ Dipartimento di Ingegneria dell'Informazione, Università degli Studi di Brescia, Via Branze 38, 25123 Brescia, Italy; fabio.mangini@unibs.it
 - ⁵ Consorzio Nazionale Interuniversitario per le Telecomunicazioni (CNIT), Viale G.P. Usberti 181/A Sede Scientifica di Ingegneria-Palazzina 3, 43124 Parma, Italy
 - ⁶ Laboratorio Europeo di Spettroscopia Nonlineare (LENS), Via Nello Carrara 1, 50019 Sesto Fiorentino, Italy; pattelli@lens.unifi.it
 - ⁷ Istituto Nazionale di Ricerca Metrologica (INRiM), Strada delle Cacce 91, 10135 Torino, Italy
- * Correspondence: andrea.tognazzi@unipa.it
† These authors contributed equally to this work.

Abstract: Dielectric metasurfaces have emerged as a promising alternative to their plasmonic counterparts due to lower ohmic losses, which hinder sensing applications and nonlinear frequency conversion, and their larger flexibility to shape the emission pattern in the visible regime. To date, the computational cost of full-wave numerical simulations has forced the exploitation of the Floquet theorem, which implies infinitely periodic structures, in designing such devices. In this work, we show the potential pitfalls of this approach when considering finite-size metasurfaces and beam-like illumination conditions, in contrast to the typical infinite plane-wave illumination compatible with the Floquet theorem.

Keywords: all-dielectric metasurfaces; multipolar decomposition; T-matrix; BIC



Citation: Ciarella, L.; Tognazzi, A.; Mangini, F.; De Angelis, C.; Pattelli, L.; Frezza, F. Finite-Size and Illumination Conditions Effects in All-Dielectric Metasurfaces. *Electronics* **2022**, *11*, 1017. <https://doi.org/10.3390/electronics11071017>

Academic Editor: Longqing Cong

Received: 14 February 2022

Accepted: 21 March 2022

Published: 24 March 2022

Publisher's Note: MDPI stays neutral with regard to jurisdictional claims in published maps and institutional affiliations.



Copyright: © 2022 by the authors. Licensee MDPI, Basel, Switzerland. This article is an open access article distributed under the terms and conditions of the Creative Commons Attribution (CC BY) license (<https://creativecommons.org/licenses/by/4.0/>).

1. Introduction

All-dielectric metasurfaces have recently emerged as a valid and promising alternative to their plasmonic counterparts. Their lower dissipative losses and thermal heating at optical frequencies allow working at higher pump power for nonlinear frequency generation and the performance of non-invasive sensing of biological samples [1–12]. Moreover, in all-dielectric resonators, electric and magnetic resonances can be used to engineer near and far fields, thus providing more degrees of freedom in the design of optical devices [1,13–16]. In this framework, III-V compounds have been used for second-harmonic generation, due to their non-centrosymmetric structure and their high second-order nonlinear coefficients [2–5,17–23]. Strong third-harmonic generation has been demonstrated instead with Si-based platforms [24,25]. Lately, great efforts have been made to improve the design of optical nanoresonators, either in the limit of single isolated nanoantennas or in the opposite scenario where perfect periodicity is assumed and thus the finite-size real-world structure is approximated by an infinite structure [26–28]. The two opposite situations are required in order to limit the numerical burden in the modelling when resorting to the full-wave solution of Maxwell's equations. Despite the fact that this has given very helpful guidelines, these approaches fail in the accurate design of a device, because they

unavoidably neglect the effects that are due to the size of a real device, which is necessarily finite and is often pumped by input beams exciting a limited portion of the device (see Figure 1). Such limitations become particularly relevant when considering metasurfaces supporting bound states in the continuum (BIC), which are non-radiating resonant modes in an open system that are not coupled to the radiating channels and exist only in infinite structures [29]. A common approach to obtain extremely high Q-factor resonances is to introduce a defect into a BIC-supporting metasurface (e.g., by breaking its symmetry), thus realizing a so-called quasi-BIC. This approach is mainly dictated by the fact that currently available simulation tools allow only infinite structures to be inspected, and thus it is necessary to break the symmetry in order to couple to such modes. Quasi-BICs, however, are expected to arise naturally by simply considering the finite extent of a real metasurface.

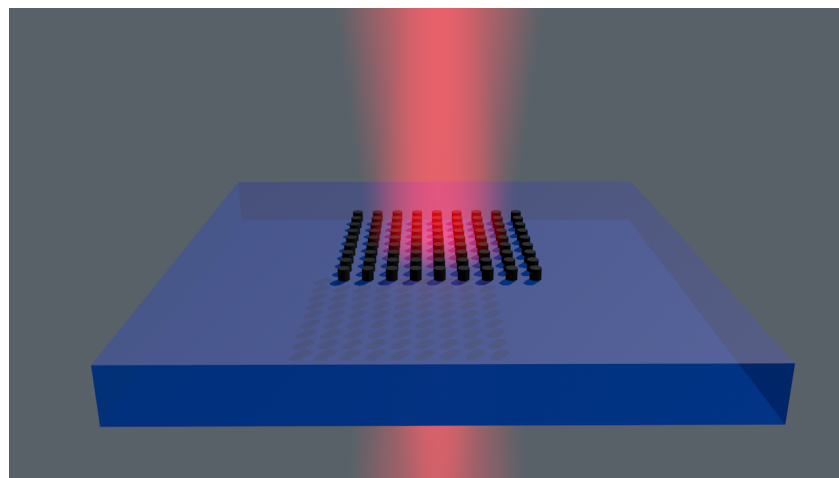


Figure 1. Sketch of a finite-size metasurface on a substrate illuminated by a Gaussian beam. Only a portion of the array is covered by the impinging light.

The necessity of using a finite-size model arises from the fact that the currently adopted models simulate an elementary unit cell and exploit the periodicity of the structure through Floquet's theorem to obtain the optical parameters of an infinite extended metasurface. The results of these models are very good, but they do not take into account the finiteness of the structure and the border effects. Furthermore, when Floquet's theorem is employed, the only possible excitation is a plane wave, unlike in experiments, where a Gaussian beam is usually employed. The combination of the two types of models can help to better foresee the behaviour of an actual metasurface in the experimental phase.

The differences between an infinite model and a finite one are highlighted in [30] and [31], where the situation is analysed with a dipole coupling model for a 2D array of nanoparticles. However, dielectric resonators often support higher-order resonances which cannot be described in the dipole approximation. In order to overcome this limitation, it is necessary to account for higher-order multipolar components, which are of particular interest for dielectric metasurfaces and the study of metamaterials in general [26,32–35]. Babicheva and Evlyukhin [36] provided an analytical model to include a quadrupolar contribution, but the authors employed an infinite structure approximation. In [37], the authors employed the superposition T-matrix scheme with the Ewald sum formalism to describe periodic structures with large unit cells. In [38], the authors studied finite-size effects in plasmonic metasurfaces, highlighting the full-width half-maximum dependence of resonances upon the number of resonators.

Our study aims to highlight the importance of the spatial finiteness of a metasurface supporting high-order multipole components. For this purpose, we employed SMUTHI [39], which implements a linear space-limited model, and tested its performance considering a metasurface composed of silicon nanopillars on a silicon oxide substrate. We analysed the total reflectivity behaviour as a function of the incident wavelength and compared it

with the results obtained with the COMSOL infinite periodic model. The reflectivity of the metasurface strongly depends on the number of elements and converges to the infinite array approximation for a large array size, thus highlighting the importance of considering the finiteness of the metasurface. Furthermore, this approach allows the metasurface to be illuminated with a Gaussian beam of a different size under the paraxial approximation, which is not possible when employing Floquet's theorem.

2. Methods

We simulated an all-dielectric metasurface composed of Si cylinders on a SiO₂ substrate, both with a periodic model using COMSOL (exploiting the periodicity via Floquet's theorem) and a space-limited model using SMUTHI, which allowed us to simulate very large finite structures due to the lower computational power required. To test the finite model, we calculated the reflectivity (R) for both models, varying the wavelength of the incident wave λ from 1250 nm to 1800 nm, in steps of 10 nm.

The finite structure was composed of a maximum of 169 cylinders lying on the substrate in a 13×13 configuration, as seen in Figure 2. The refractive indices were 1 for the air, 3.45 for the cylinders, and 1.45 for the substrate, the last two values being the silicon and silicon oxide indices at the working frequencies. The cylinder heights were 428 nm and their radii were 214 nm. The distance between two adjacent cylinders was 856 nm. These dimensions were chosen to create a structure that supports resonant modes at the working frequencies on two levels: inside single cylinders and globally due to the periodicity. The layers consisted of a substrate with thickness $2\lambda/n_{\text{substrate}}$ and an air layer 2λ thick, and the domain on the plane of the cylinders was a square with a side length of 15,500 nm. Although SMUTHI allows the simulation of lossy media, in this study we employed a fixed real value for the refractive indices, because in the spectral region of interest the silicon and silicon dioxide absorption coefficients and the dispersion were very small and thus could be neglected.

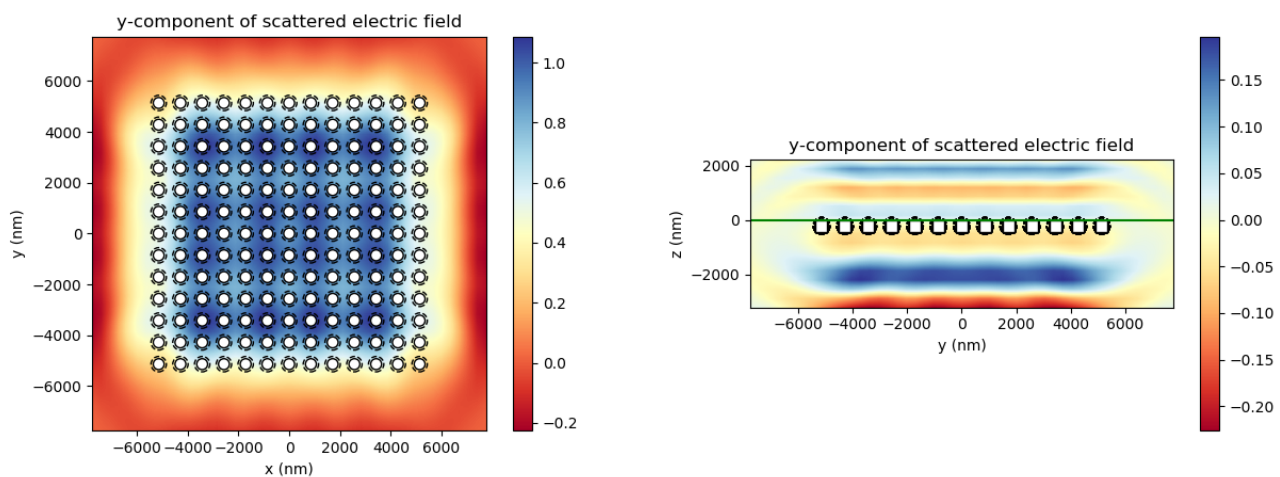


Figure 2. The y -component of the scattered electric field given by SMUTHI in the xy (left) and yz planes (right) for the structure composed of 13×13 cylinders. The substrate (positive z -axis) has $n = 1.45$ and the air layer (negative z -axis) has $n = 1$. The cylinders have $n = 3.45$, height 428 nm, and radius 214 nm, and 856 nm is the periodicity (distance between two cylinders on the same column or row). The incident wave is a Gaussian beam 15 μm wide at 1600 nm, linearly polarized along the y -axis with an initial maximum intensity of the electric field of 1 V m^{-1} , with the maximum at the origin $(x, y, z) = (0, 0, 0)$. The incidence is perpendicular to the substrate and the propagation direction is towards the positive z -direction. The domain on the xy plane is a square with a side length of 15,500 nm.

The incident wave used for the COMSOL periodic model is always a plane wave polarized along the y -axis, while with SMUTHI it is also possible to simulate an incident

Gaussian beam. We set an incident wave propagating from the air layer towards the substrate at normal incidence, at a wavelength which varied as previously described. The polarization of the wave was linear, with the electric field oscillating along the y -axis and an initial intensity of $E_0 = 1 \text{ V m}^{-1}$. The maximum value of the electric field was at the air–substrate interface. To calculate the reflectivity, we wrote a MATLAB script, which takes as an input the SMUTHI results related to the scattered field from the cylinders and the reflected one from the substrate. Then, we calculated the flux of the Poynting vector through three surfaces xy , yz , and xz at the border of the domain described above, inside the air layer.

The formulas used to evaluate the Poynting vector components were the following [40]:

$$p_x = \frac{|E_y|^2 + |E_z|^2}{2Z} \quad p_y = \frac{|E_x|^2 + |E_z|^2}{2Z}$$

$$p_z = \frac{|E_x|^2 + |E_y|^2}{2Z} \quad p_0 = \frac{|E_{0y}|^2}{2Z} = \frac{|E_0|^2}{2Z}$$

where E_x , E_y , and E_z are the field components given by the combinations of the scattered and the reflected waves, E_0 is the initial intensity, and Z is the characteristic impedance of vacuum. Integrating these values along the respective surfaces, it is possible to calculate the reflectivity:

$$R = \frac{P_z + 2P_x + 2P_y}{P_0}$$

where capital P_x , P_y , and P_z are the powers relative to the power densities with the same subscript and are obtained through surface integration over the simulation domain walls. This procedure was repeated for each wavelength to obtain the full spectrum.

3. Validation

To develop the space-limited model we used SMUTHI, a recently developed open-source Python package based on numerical methods, to speed up the computation of light scattering problems [41,42] (an analytical treatment is reported in Appendix A).

To determine how the software performs in our situation, we developed two simple models of the metasurface, one using COMSOL and the other using SMUTHI, to compare the outputs for a structure composed of nine cylinders arranged in a 3×3 configuration around the origin. The parameters were the same as those set in the previous section, except for the domain width in the plane of the cylinders, which was changed to 5000 nm, and the incident plane wave that was fixed at 1200 nm. In COMSOL, we simulated a larger domain: a cube with a side length of 6500 nm with a perfectly matched layer all around, in order to prevent unwanted reflections from the side. We performed the integration on the same surface as that employed in SMUTHI. We employed the iterative GMRES solver in COMSOL and set a mesh size of $\lambda_e/7$, where λ_e is the effective refractive index of the material.

Figure 3 shows the electric fields at a distance of 1430 nm from the last cylinder, obtained in COMSOL (left) and SMUTHI (right), respectively.

A good agreement was found using a multipolar expansion with $l = m = 3$ for the cylinders, which resulted in very similar field distributions and integrated reflectance values of:

$$R_{\text{COMSOL}} = 0.0649$$

$$R_{\text{SMUTHI}} = 0.0542$$

Then, for the transmission coefficient:

$$T_{\text{SMUTHI}} = 0.9482$$

and thus the condition $R + T = 1$ is almost respected (this must hold because the refractive indices are real) [41,42].

We underline the times required for the two simulations: for the structure reported in this chapter, COMSOL required 16 min with a reduced geometry, obtained by exploiting symmetry considerations, and 74 min with the full structure, to solve the problem; on the other hand, SMUTHI required 3 min (PC specifications: CPU Intel® Xeon® E5-2650 0, 2 GHz, 8 core. RAM DIMM-DD3 1600 MHz, 64 GB. GPU NVIDIA Quadro K2000). Although COMSOL provides a more complete simulation by computing the field in the full volume of the structure, we only need the field on three specific surfaces, and thus SMUTHI is much more time-efficient.

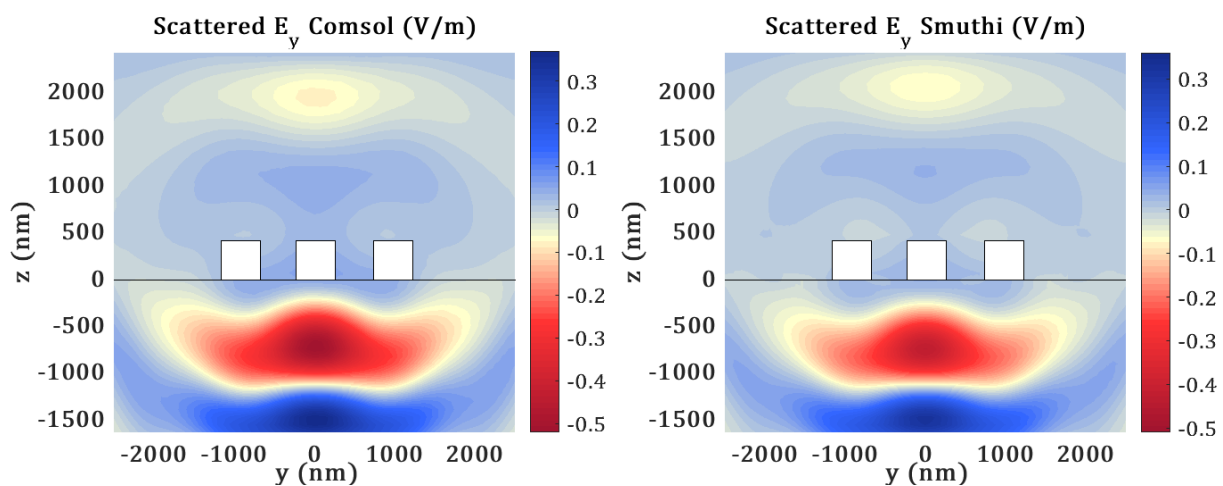


Figure 3. The y -component of the scattered electric field obtained with COMSOL (left) and with SMUTHI (right) for the structure composed of 3×3 cylinders. The cylinders have $n = 3.45$, height 428 nm, and radius 214 nm, with 856 nm as the periodicity. The incident wave is a plane wave at 1200 nm, linearly polarized along the y -axis at normal incidence. The domain on the xy plane is a square with a side length of 5000 nm. The plots are along the yz plane at a distance of 1430 nm from the last cylinders (2500 nm from the centre of the structure).

4. Results

Figure 4a shows the plots of R , calculated on the same surface, as a function of the wavelength, for different metasurface sizes. When the number of cylinders increases, the spectral features related to the multipolar resonances inside the cylinders and their interplay become more evident. We note that for smaller arrays, the covered area inside the integration surface is much smaller, thus resulting in smaller reflectivity values.

In Figure 4b–d we compare the reflectivity as a function of the wavelength obtained with the two models.

For the finite-size model, the values are relative to the 13×13 cylinder structure and are normalized to have a maximum equal to one. The normalization is only for comparison purposes. Indeed, in the finite structure case, when the integration domain is enlarged, the unpatterned surface increases, thus reducing the reflectivity. However, the relative size of the peaks does not change as this is only due to the cylinders. The normalization of the finite structure to the infinite structure allows the relative intensities of the peaks to be compared, and thus the finite-size effect to be evaluated. We compared the spectra with an incident plane wave for both structures and then changed the wave for the finite model into a Gaussian beam 15 μm and 6 μm wide. Our simulations showed that as long

as the paraxial simulation holds and the beam covers the metasurface, the plane wave approximation deviates slightly from the real situation.

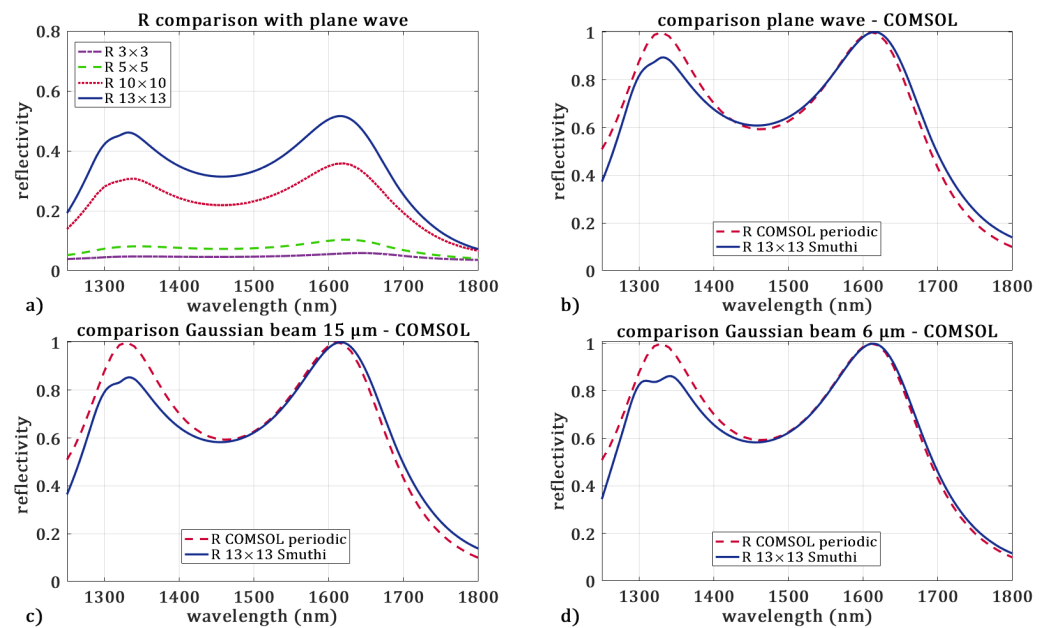


Figure 4. Reflectivity (R) as a function of the wavelength for both the periodic model and the finite model. (a) R as a function of the wavelength for the structures obtained by varying the number of cylinders (3×3 , 5×5 , 10×10 , and 13×13), simulated with SMUTHI. The integration surface is the same for all the structures. (c,d) Comparisons between the two models. For the periodic model with COMSOL, the incident wave is a plane wave; for the space-limited model with SMUTHI there is an incident plane wave (b), an incident Gaussian beam 15 μm wide (c), and an incident Gaussian beam 6 μm wide (d). The values obtained with SMUTHI are normalized so that the maximum is equal to one.

The normalized behaviours are very faithful to the COMSOL behaviours, either with an incident plane wave or with a Gaussian beam. In particular, we see two peaks at 1610 nm and 1330 nm, which are at exactly the same wavelengths for the two models. The resonance at 1610 nm is related to the magnetic dipole inside the cylinder and is also present in the scattering cross section in the isolated structure. The different values around the shorter wavelength peak are due to the finite extension of the structure and the excitation beam; therefore, this feature can only be highlighted through a finite-size model. Indeed, a Gaussian beam can be described by considering a larger amount of k -vectors, which is not possible with the plane-wave excitation employed in COMSOL. This is further evident from Figure 5, where we report also the results obtained considering the flux through the walls around the central cylinder in the finite-size model and the reflectivity of the infinite periodic structure. It is interesting to note that the characteristic of the bigger structure is more similar to the periodic model. As expected, the relative weight of the resonant peak due to the interaction between the cylinders (around 1330 nm) and the single-pillar magnetic dipole (1610 nm) increases with the array size. We emphasize that the resonance at 1610 nm is related to the magnetic dipole in the isolated pillar, thus it is well reproduced even for small arrays and beam sizes. Thus, these results show that it is essential to consider the size of the system and the excitation, to correctly describe a real finite-size system. For this purpose, it should be noted that the size of the structure compared to the wavelength is more important than the number of unit cells considered in the simulation. However, the size of the unit cells plays a key role in determining the interaction strength between the resonators. Indeed, if the cylinders are well separated from each other, they act as isolated

sources, and the scattering properties can be evaluated by computing the electromagnetic field of an isolated pillar and considering the system as an array of antennas.

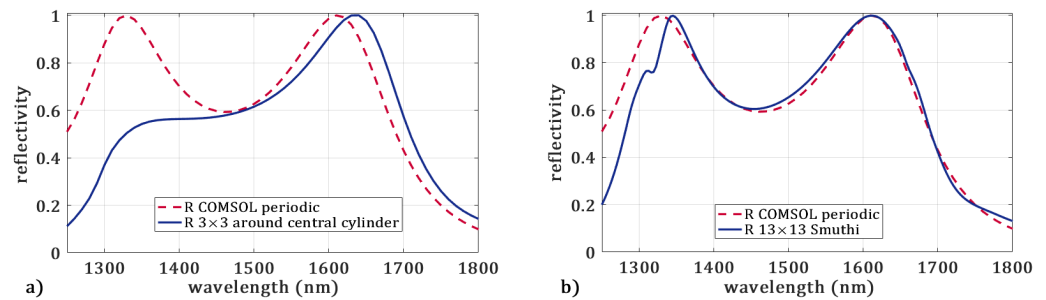


Figure 5. Reflectivity as a function of the wavelength for infinite case (dashed lines) and finite case (continuous lines). For the finite case, the power flux is considered through the walls around the central cylinder for the structures with 3×3 cylinders (a) and 13×13 cylinders (b). This means that the simulation domain on the xy plane has a width of 856 nm around the central cylinder (compared to the previous value of 15,500 nm). The plots obtained with SMUTHI are normalized to have a maximum equal to one.

To further prove the importance of finite-size effects in conjunction with resonant behaviour, we consider a structure supporting bound states in the continuum. Figure 6 shows the reflectivity as a function of the wavelength for a suspended array of cylinders, which was previously reported for sustaining a BIC [43]. The Gaussian beam waist was kept fixed at $10 \mu\text{m}$, while the number of resonators was increased. It is clear that increasing the number of resonators reduces the line width of the Fano resonance associated with the quasi-BIC. We highlight that in [43], the authors introduced a gap in the middle of the cylinders in order to couple to the resonant mode, while in our case this was not necessary since both the illumination and the structure were finite and the modes could couple to the radiating channels.

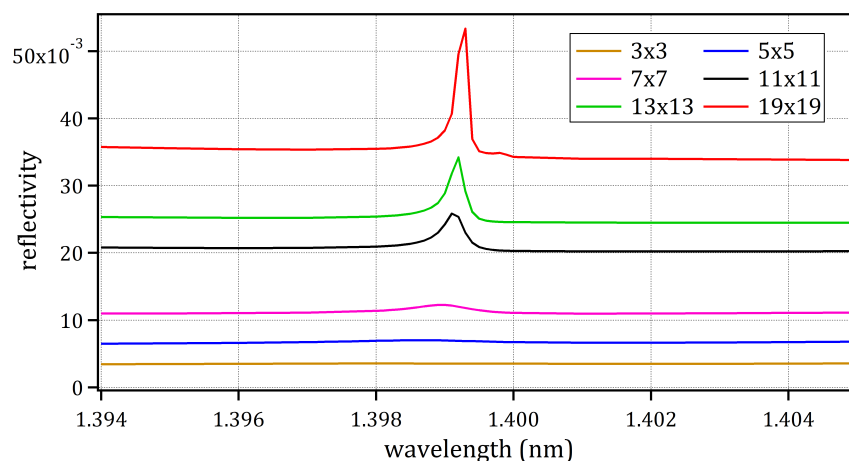


Figure 6. Reflectivity as a function of wavelength for arrays of cylinders (height 563 nm, radius 250 nm, and period 850 nm) with different numbers of elements. The refractive index is 3.49 and the impinging Gaussian beam waist is $10 \mu\text{m}$.

5. Conclusions

In conclusion, we built a space-limited model with SMUTHI to simulate a real metasurface, to determine the border effects. First, we tested the software performance in the presence of the metasurface and verified the conservation of energy in the simulated domain ($R + T = 1$), as well as the agreement with the COMSOL simulation. The resulting

reflection coefficients R were similar for the two structures, and the produced scattered fields were very similar.

We developed the finite model by introducing an approximation for the scattered field and the refractive indices. Moreover, with the finite-domain model, it was possible to highlight a difference in the higher-frequency peak related to collective excitation. We could also simulate an incident Gaussian beam, which is not possible in the periodic case. SMUTHI allowed us to simulate the wavelength sweep for a large finite structure with 13×13 cylinders, which is impractical to replicate in COMSOL, and also allowed us to simulate the configuration with 3×3 cylinders 5.3 times faster. This approach also allowed us to employ a non-periodic distribution of resonators, which is not possible when exploiting the Floquet theorem. Furthermore, it allowed us to study real situations involving BIC, which are intimately related to the finiteness of the system. The proposed approach may be further extended by analogy with [44], where the authors employed multipolar decomposition to study free-standing single nanoparticles, to simulate nonlinear frequency generation in finite-size metasurfaces.

Author Contributions: Conceptualization, F.M. and A.T.; methodology, L.P.; software, L.P.; investigation, L.C., A.T., F.M. and L.P.; writing—original draft preparation, L.C. and A.T.; writing—review and editing, all the authors contributed equally; supervision, F.F. and C.D.A.; funding acquisition, C.D.A. All authors have read and agreed to the published version of the manuscript.

Funding: This research was funded by Ministero dell’Istruzione, dell’Università e della Ricerca through the PRIN project “NOMEN” (project 2017MP7F8F), the European community through the “METAFAST” project (H2020-FETOPEN-2018-2020, grant agreement no. 899673), and NATO through the Science for Peace and Security (SPS) Programme, project “OPTIMIST” (SPS G5850). L.P. acknowledges Progetto Premiale MIUR “Volume photography” and NVIDIA Corporation for the donation of the Titan X Pascal GPU used for this research.

Acknowledgments: The authors thank Amos Egel for fruitful discussions. The authors are grateful for the financial support of MIUR through the PRIN project “NOMEN” (project 2017MP7F8F), the European community through the “METAFAST” project (H2020-FETOPEN-2018-2020, grant agreement no. 899673), and NATO through the Science for Peace and Security (SPS) Programme, project “OPTIMIST” (SPS G5850). L.P. acknowledges Progetto Premiale MIUR “Volume photography” and NVIDIA Corporation for the donation of the Titan X Pascal GPU used for this research.

Conflicts of Interest: The authors declare no conflict of interest.

Appendix A. Scattering from Axially Symmetric Particles on a Stratified Medium

The SMUTHI software allows the resolution of the electromagnetic scattering problem from an ensemble of axially symmetric particles in a stratified medium. To approach this problem, SMUTHI uses a combination of methods that include the expansion of spherical vector wave functions (SVWFs) to represent the impinging wave in spherical waves, the expansion of plane vector wave functions (PVWFs) to represent the spherical wave in a complete set of plane waves, in order to consider the interaction between the scattered field from the particle and the stratified medium, and a T-matrix approach (or null-field method) with the addition theorem to take into account the interaction between each scatterer. The first step of the method consists of the representation of all the fields as an expansion of SVWFs, then, fixing a scatterer s , they can be written as a superposition of regular harmonic functions for the incoming field or with outgoing harmonic functions [41,42,45–53]:

$$\mathbf{E}_{reg}^s(\mathbf{r}) = \sum_n a_n^s \mathbf{M}_n^{(1)}(\mathbf{r} - \mathbf{r}_s) \quad (\text{A1})$$

$$\mathbf{E}_{sca}^s(\mathbf{r}) = \sum_n b_n^s \mathbf{M}_n^{(3)}(\mathbf{r} - \mathbf{r}_s) \quad (\text{A2})$$

where the apexes (1) and (3) represent the types of the SVWFs. In particular, the first type of the Bessel spherical function is used as the harmonic function with (1) and the third type of the same function is used with (3). Each one is centred in the middle of the particle \mathbf{r}_s . The second step consists of the simultaneous calculation of the coefficients for the incoming and outgoing fields for each scatterer s . For this, we use the null-field method and the addition theorem, obtaining:

$$b_n^s = \sum_{n'} T_{nn'}^s a_{n'}^s \quad (\text{A3})$$

$$a_n^s = \sum_{s'} \sum_{n'} W_{nn'}^{ss'} b_{n'}^{s'} a_n^{s,in} \quad (\text{A4})$$

having indicated with $T_{nn'}^s$ the T-matrix for a single scatterer, and with the matrix $W_{nn'}^{ss'}$ the mutual interaction between the particles, using the addition theorem and the stratified medium. The third step is characterized by the determination of the interaction between the ensemble of the scattering particles and the stratified medium. The coupling matrix $W_{nn'}^{ss'}$ can be found by considering the superposition of two contributions:

$$W_{nn'}^{ss'} = W_{nn'}^{D,ss'} + W_{nn'}^{R,ss'} \quad (\text{A5})$$

where the first is the coupling term for an infinite medium and the second represents the (multiple) reflections of the wave at the layer interfaces, which are then the incident fields to the particle s . In particular, the last term can be expressed as an expansion of PVWFs, given the flat nature of the interface. Using the Sommerfeld integration form we have:

$$W_{nn'}^{R,ss'} = 4i^{|m'-m|} e^{i|m'-m|} \varphi_{s's} \int_0^\infty [(f_{nn'}^+(K, z) + f_{nn'}^-(K, z)) J_{|m'-m|(k\rho)} dK] \quad (\text{A6})$$

with

$$f_{nn'}^+(k, z) = \frac{K}{k_z k} \sum_j [B_{n,j}^+(L_j^{is})_{12} B_{n',j}^- e^{ik_z z} + B_{n,j}^-(L_j^{is})_{21} B_{n',j}^+ e^{-ik_z z}] \quad (\text{A7})$$

$$f_{nn'}^-(k, z) = \frac{K}{k_z k} \sum_j [B_{n,j}^+(L_j^{is})_{11} B_{n',j}^- e^{ik_z z} + B_{n,j}^-(L_j^{is})_{22} B_{n',j}^+ e^{-ik_z z}] \quad (\text{A8})$$

where j indicates the plane wave TE- or TH-polarization, k , K , and k_z are the wavenumber, the wave vector's radial cylinder and the z component in the scattering particle surface, respectively, $B_{n,j}^{\pm}$ are the transformation coefficients in matrix form between the SVWFs and PVWFs, and L_j^{is} is a generalized reflection coefficient in matrix form encoding the overall response of the flat layer interfaces. A complete derivation of the values can be found in [41,42,45–53].

References

1. Kuznetsov, A.I.; Miroshnichenko, A.E.; Brongersma, M.L.; Kivshar, Y.S.; Luk'yanchuk, B. Optically resonant dielectric nanostructures. *Science* **2016**, *354*, aag2472. [CrossRef] [PubMed]
2. Carletti, L.; Locatelli, A.; Stepanenko, O.; Leo, G.; De Angelis, C. Enhanced second-harmonic generation from magnetic resonance in AlGaAs nanoantennas. *Opt. Express* **2015**, *23*, 26544. [CrossRef] [PubMed]
3. Gili, V.F.; Carletti, L.; Locatelli, A.; Rocco, D.; Finazzi, M.; Ghirardini, L.; Favero, I.; Gomez, C.; Lemaître, A.; Celebrano, M.; et al. Monolithic AlGaAs second-harmonic nanoantennas. *Opt. Express* **2016**, *24*, 15965. [CrossRef] [PubMed]
4. Liu, S.; Sinclair, M.B.; Saravi, S.; Keeler, G.A.; Yang, Y.; Reno, J.; Peake, G.M.; Setzpfandt, F.; Staude, I.; Pertsch, T.; et al. Resonantly Enhanced Second-Harmonic Generation Using III-V Semiconductor All-Dielectric Metasurfaces. *Nano Lett.* **2016**, *16*, 5426–5432. [CrossRef]
5. Ghirardini, L.; Carletti, L.; Gili, V.; Pellegrini, G.; Duò, L.; Finazzi, M.; Rocco, D.; Locatelli, A.; De Angelis, C.; Favero, I.; et al. Polarization properties of second-harmonic generation in AlGaAs optical nanoantennas. *Opt. Lett.* **2017**, *42*, 559–562. [CrossRef]

6. Marino, G.; Solntsev, A.S.; Xu, L.; Gili, V.; Carletti, L.; Poddubny, A.N.; Smirnova, D.; Chen, H.; Zhang, G.; Zayats, A.; et al. Sum-frequency generation and photon-pair creation in AlGaAs nano-scale resonators. In Proceedings of the 2017 Conference on Lasers and Electro-Optics (CLEO), San Jose, CA, USA, 14–19 May 2017.
7. Smirnova, D.; Kivshar, Y.S. Multipolar nonlinear nanophotonics. *Optica* **2016**, *3*, 1241–1255. doi: 10.1364/optica.3.001241. [\[CrossRef\]](#)
8. Lapine, M. New degrees of freedom in nonlinear metamaterials. *Phys. Status Solidi (B) Basic Res.* **2017**, *254*, 1600462. [\[CrossRef\]](#)
9. Krasnok, A.; Tymchenko, M.; Alù, A. Nonlinear metasurfaces: A paradigm shift in nonlinear optics. *Mater. Today* **2018**, *21*, 8–21.
10. Heydari, S.; Bazgir, M.; Zarrabi, F.B.; Gandji, N.P.; Rastan, I. Novel optical polarizer design based on metasurface nano aperture for biological sensing in mid-infrared regime. *Opt. Quantum Electron.* **2017**, *49*, 83. [\[CrossRef\]](#)
11. Ebrahimi, S.; Poorgholam-Khanjari, S. Highly Q-factor optical metasurface based on DNA nanorods with Fano response for on-chip optical sensing. *Optik* **2021**, *232*, 166576. doi: 10.1016/j.ijleo.2021.166576. [\[CrossRef\]](#)
12. Mobasser, S.; Poorgholam-Khanjari, S.; Bazgir, M.; Zarrabi, F.B. Highly Sensitive Reconfigurable Plasmonic Metasurface with Dual-Band Response for Optical Sensing and Switching in the Mid-Infrared Spectrum. *J. Electron. Mater.* **2021**, *50*, 120–128. [\[CrossRef\]](#)
13. Krasnok, A.; Savelev, R. All-Dielectric Nanophotonics: Fundamentals, Fabrication and Applications. In *World Scientific Handbook of Metamaterials and Plasmonics-Volume 1*; Mayer, S., Ed.; World Scientific: Singapore, 2017; Chapter 8, pp. 337–385.
14. Jahani, S.; Jacob, Z. All-dielectric metamaterials. *Nat. Nanotechnol.* **2016**, *11*, 23–36. [\[CrossRef\]](#) [\[PubMed\]](#)
15. Zhao, Q.; Zhou, J.; Zhang, F.; Lippens, D. Mie resonance-based dielectric metamaterials. *Mater. Today* **2009**, *12*, 60–69. [\[CrossRef\]](#)
16. Chen, H.T.; Taylor, A.J.; Yu, N. A review of metasurfaces: Physics and applications. *Rep. Prog. Phys.* **2016**, *79*.
17. Carletti, L.; Rocco, D.; Locatelli, A.; De Angelis, C.; Gili, V.F.; Ravaro, M.; Favero, I.; Leo, G.; Finazzi, M.; Ghirardini, L.; et al. Controlling second-harmonic generation at the nanoscale with monolithic AlGaAs-on-AlOx antennas. *Nanotechnology* **2017**, *28*, 114005. [\[CrossRef\]](#)
18. Carletti, L.; Marino, G.; Ghirardini, L.; Gili, V.F.; Rocco, D.; Favero, I.; Locatelli, A.; Zayats, A.V.; Celebrano, M.; Finazzi, M.; et al. Nonlinear Goniometry by Second-Harmonic Generation in AlGaAs Nanoantennas. *ACS Photonics* **2018**, *5*, 4386–4392. [\[CrossRef\]](#)
19. Carletti, L.; Locatelli, A.; Neshev, D.; De Angelis, C. Shaping the Radiation Pattern of Second-Harmonic Generation from AlGaAs Dielectric Nanoantennas. *ACS Photonics* **2016**, *3*, 1500–1507. [\[CrossRef\]](#)
20. Camacho-Morales, R.; Rahmani, M.; Kruk, S.; Wang, L.; Xu, L.; Smirnova, D.A.; Solntsev, A.S.; Miroshnichenko, A.; Tan, H.H.; Karouta, F.; et al. Nonlinear Generation of Vector Beams from AlGaAs Nanoantennas. *Nano Lett.* **2016**, *16*, 7191–7197. [\[CrossRef\]](#)
21. Kruk, S.S.; Camacho-Morales, R.; Xu, L.; Rahmani, M.; Smirnova, D.A.; Wang, L.; Tan, H.H.; Jagadish, C.; Neshev, D.N.; Kivshar, Y.S. Nonlinear optical magnetism revealed by second-harmonic generation in nanoantennas. *Nano Lett.* **2017**, *17*, 3914–3918. [\[CrossRef\]](#)
22. Shcherbakov, M.R.; Vabishchevich, P.P.; Shorokhov, A.S.; Chong, K.E.; Choi, D.Y.; Staude, I.; Miroshnichenko, A.E.; Neshev, D.N.; Fedyanin, A.A.; Kivshar, Y.S. Ultrafast All-Optical Switching with Magnetic Resonances in Nonlinear Dielectric Nanostructures. *Nano Lett.* **2015**, *15*, 6985–6990. [\[CrossRef\]](#)
23. Della Valle, G.; Hopkins, B.; Ganzer, L.; Stoll, T.; Rahmani, M.; Longhi, S.; Kivshar, Y.S.; De Angelis, C.; Neshev, D.N.; Cerullo, G. Nonlinear Anisotropic Dielectric Metasurfaces for Ultrafast Nanophotonics. *ACS Photonics* **2017**, *4*, 2129–2136. [\[CrossRef\]](#)
24. Shcherbakov, M.R.; Neshev, D.N.; Hopkins, B.; Shorokhov, A.S.; Staude, I.; Melik-Gaykazyan, E.V.; Decker, M.; Ezhov, A.A.; Miroshnichenko, A.E.; Brener, I.; et al. Enhanced third-harmonic generation in silicon nanoparticles driven by magnetic response. *Nano Lett.* **2014**, *14*, 6488–6492. [\[CrossRef\]](#) [\[PubMed\]](#)
25. Yang, Y.; Wang, W.; Boulesbaa, A.; Kravchenko, I.I.; Briggs, D.P.; Poretzky, A.; Geohegan, D.; Valentine, J. Nonlinear Fano-Resonant Dielectric Metasurfaces. *Nano Lett.* **2015**, *15*, 7388–7393. [\[CrossRef\]](#) [\[PubMed\]](#)
26. Babicheva, V.E.; Evlyukhin, A.B. Multipole lattice effects in high refractive index metasurfaces. *J. Appl. Phys.* **2021**, *129*, 040902.
27. Castellanos, G.W.; Bai, P.; Gómez Rivas, J. Lattice resonances in dielectric metasurfaces. *J. Appl. Phys.* **2019**, *125*, 213105.
28. Utyushev, A.D.; Zakomirnyi, V.I.; Ershov, A.E.; Gerasimov, V.S.; Karpov, S.V.; Rasskazov, I.L. Collective Lattice Resonances in All-Dielectric Nanostructures under Oblique Incidence. *Photonics* **2020**, *7*, 24. [\[CrossRef\]](#)
29. Joseph, S.; Pandey, S.; Sarkar, S.; Joseph, J. Bound states in the continuum in resonant nanostructures: An overview of engineered materials for tailored applications. *Nanophotonics* **2021**, *10*, 4175–4207. doi: 10.1515/nanoph-2021-0387. [\[CrossRef\]](#)
30. Zundel, L.; Manjavacas, A. Finite-size effects on periodic arrays of nanostructures. *J. Phys. Photonics* **2018**, *1*, 015004.
31. Zakomirnyi, V.I.; Ershov, A.E.; Gerasimov, V.S.; Karpov, S.V.; Ågren, H.; Rasskazov, I.L. Collective lattice resonances in arrays of dielectric nanoparticles: a matter of size. *Opt. Lett.* **2019**, *44*, 5743–5746. [\[CrossRef\]](#)
32. Zakomirnyi, V.I.; Karpov, S.V.; Ågren, H.; Rasskazov, I.L. Collective lattice resonances in disordered and quasi-random all-dielectric metasurfaces. *J. Opt. Soc. Am. B* **2019**, *36*, E21–E29. [\[CrossRef\]](#)
33. Ziolkowski, R.W. Mixtures of Multipoles—Should They Be in Your EM Toolbox? *IEEE Open J. Antennas Propag.* **2022**, *3*, 154–188. [\[CrossRef\]](#)
34. Czajkowski, K.M.; Bancerek, M.; Antosiewicz, T.J. Multipole analysis of substrate-supported dielectric nanoresonator metasurfaces via the *T*-matrix method. *Phys. Rev. B* **2020**, *102*, 085431. [\[CrossRef\]](#)
35. Li, J.; Verellen, N.; Van Dorpe, P. Engineering electric and magnetic dipole coupling in arrays of dielectric nanoparticles. *J. Appl. Phys.* **2018**, *123*, 083101.

36. Babicheva, V.E.; Evlyukhin, A.B. Analytical model of resonant electromagnetic dipole-quadrupole coupling in nanoparticle arrays. *Phys. Rev. B* **2019**, *99*, 195444. [[CrossRef](#)]
37. Theobald, D.; Beutel, D.; Borgmann, L.; Mescher, H.; Gomard, G.; Rockstuhl, C.; Lemmer, U. Simulation of light scattering in large, disordered nanostructures using a periodic T-matrix method. *J. Quant. Spectrosc. Radiat. Transf.* **2021**, *272*, 107802. [[CrossRef](#)]
38. Kostyukov, A.S.; Rasskazov, I.L.; Gerasimov, V.S.; Polyutov, S.P.; Karpov, S.V.; Ershov, A.E. Multipolar Lattice Resonances in Plasmonic Finite-Size Metasurfaces. *Photonics* **2021**, *8*, 109. [[CrossRef](#)]
39. Egel, A.; Czajkowski, K.M.; Theobald, D.; Ladutenko, K.; Kuznetsov, A.S.; Pattelli, L. SMUTHI: A python package for the simulation of light scattering by multiple particles near or between planar interfaces. *J. Quant. Spectrosc. Radiat. Transf.* **2021**, *273*, 107846. doi:10.1016/j.jqsrt.2021.107846. [[CrossRef](#)]
40. Sharma, K.K. *Optics: Principles and Applications*, 1st ed.; Academic Press: Cambridge, MA, USA, 2006.
41. Egel, A.; Kettlitz, S.W.; Lemmer, U. Efficient evaluation of Sommerfeld integrals for the optical simulation of many scattering particles in planarly layered media. *J. Opt. Soc. Am. A* **2016**, *33*, 698–706. [[CrossRef](#)]
42. Egel, A.; Lemmer, U. Dipole emission in stratified media with multiple spherical scatterers: Enhanced outcoupling from OLEDs. *J. Quant. Spectrosc. Radiat. Transf.* **2014**, *148*, 165–176. [[CrossRef](#)]
43. Tognazzi, A.; Rocco, D.; Gandolfi, M.; Locatelli, A.; Carletti, L.; De Angelis, C. High Quality Factor Silicon Membrane Metasurface for Intensity-Based Refractive Index Sensing. *Optics* **2021**, *2*, 193–199. [[CrossRef](#)]
44. Smirnova, D.A.; Khanikaev, A.B.; Smirnov, L.A.; Kivshar, Y.S. Multipolar Third-Harmonic Generation Driven by Optically Induced Magnetic Resonances. *ACS Photonics* **2016**, *3*, 1468–1476.
45. Videen, G. Light scattering from a particle on or near a perfectly conducting surface. *Opt. Commun.* **1995**, *115*, 1–7. [[CrossRef](#)]
46. Wriedt, T.; Doicu, A. Light scattering from a particle on or near a surface. *Opt. Commun.* **1998**, *152*, 376–384. [[CrossRef](#)]
47. Tsang, L.; Kong, J.A.; Ding, K.H. *Scattering of Electromagnetic Waves. Theory and Applications*, 1st ed.; Wiley: Hoboken, NJ, USA, 2000.
48. Doicu, A.; Wriedt, T.; Eremin, Y.A. *Light Scattering by Systems of Particles*, 1st ed.; Springer: Berlin/Heidelberg, Germany, 2006.
49. Frezza, F.; Mangini, F.; Pajewski, L.; Schettini, G.; Tedeschi, N. Spectral domain method for the electromagnetic scattering by a buried sphere. *J. Opt. Soc. Am. A* **2013**, *30*, 783–790. [[CrossRef](#)] [[PubMed](#)]
50. Frezza, F.; Mangini, F.; Tedeschi, N. Electromagnetic scattering by two concentric spheres buried in a stratified material. *J. Opt. Soc. Am. A* **2015**, *32*, 277–286. [[CrossRef](#)]
51. Frezza, F.; Mangini, F. Vectorial spherical-harmonics representation of an inhomogeneous elliptically polarized plane wave. *J. Opt. Soc. Am. A* **2015**, *32*, 1379–1383. [[CrossRef](#)]
52. Frezza, F.; Mangini, F. Electromagnetic scattering by a buried sphere in a lossy medium of an inhomogeneous plane wave at arbitrary incidence: Spectral-domain method. *J. Opt. Soc. Am. A* **2016**, *33*, 947–953. [[CrossRef](#)]
53. Frezza, F.; Mangini, F. Electromagnetic scattering of an inhomogeneous elliptically polarized plane wave by a multilayered sphere. *J. Electromagn. Waves Appl.* **2016**, *30*, 492–504. [[CrossRef](#)]